SUPPLEMENTARY MATERIAL

Ecogeographic connectivity shaped the earliest hominin presence and access route in the Iberian Peninsula

Juan José González-Quiñones[1], Juan Francisco Reinoso-Gordo[1], Pedro Matias[2], Vitor Santos[3], Hugues-Alexandre Blain[4,5], Juan Manuel Jiménez-Arenas[6,7,8]

[1] Department of Architectural and Engineering Graphic Expression, University of Granada, Spain; juanjosegonzalez@ugr.es, jreinoso@ugr.es

[2] Universidade Lusófona, RCM2+ Centro de Investigação em Gestão de Ativos e Engenharia de Sistemas, Campo Grande, 376, 1749-024, Lisboa, Portugal; pedro.matias@ulusofona.pt

[3] NOVA Information Management School, Information Management Research Center (MagIC), Lisboa, Portugal; vsantos@novaims.unl.pt

[4] Institut Català de Paleoecologia Humana i Evolució Social (IPHES-CERCA), Tarragona, Spain; hablain@iphes.cat

[5] Department of History and History of Art, University Rovira i Virgili, Tarragona, Spain;

[6] Department of Prehistory and Archaeology, University of Granada, Spain; jumajia@ugr.es

[7] Unit of Excellence Archaeometrical Studies. Inside the artefacts & ecofacts, University of Granada, Spain

[8] Research Group HUM1103 Quaternary and human evolution in Africa and southern Iberia (CUATE), Junta de Andalucía

Index

Figures

Tables

Text

Video

FIGURES

Figure S1

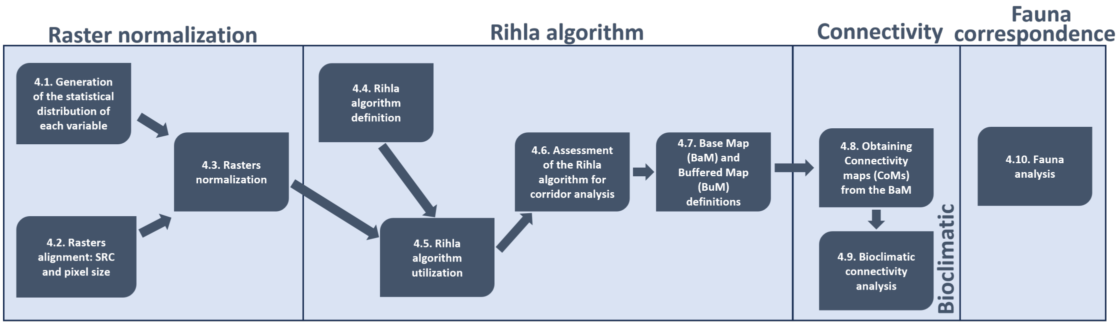

Figure S1. Workflow method. The proposed model is organized into four main blocks: raster normalization, where MAT, MAP, woodland cover, and slope are standardized to values between 0 and 1 according to their potential for hominin presence; the Rihla algorithm, which integrates these variables into a pathfinding procedure and evaluates the reliability of the resulting routes; connectivity, based on an inferred base map of trodden paths used to calculate connections between archaeological sites and climate zones; and faunal correspondence, assessed through the Jaccard index and UPGMA clustering.

Figure S2

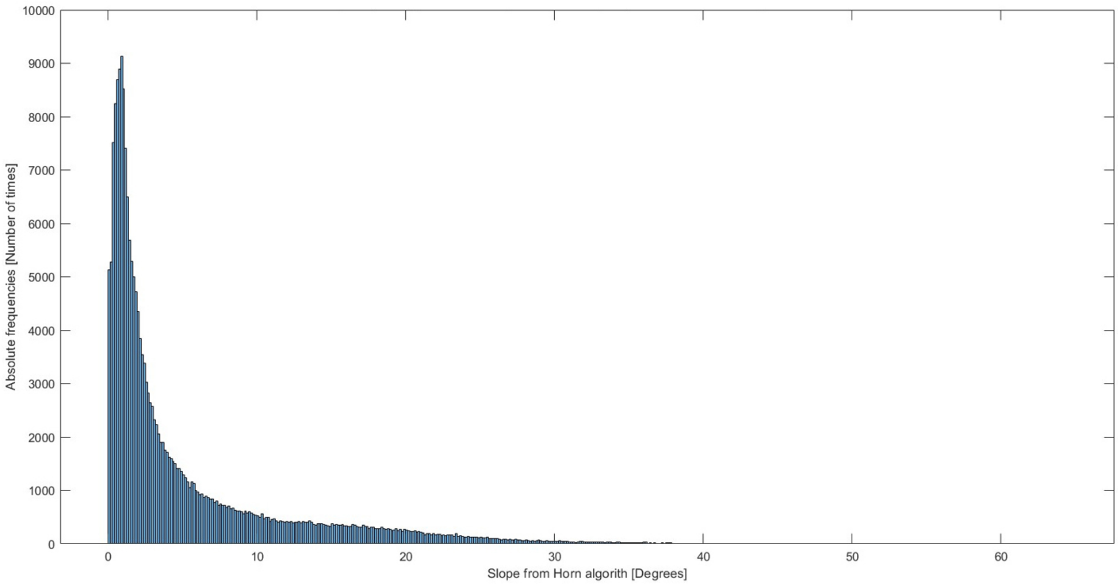

Figure S2. Histogram of slopes in the areas of influence of the 26 archaeological sites with known coordinates and human presence from the Early Pleistocene. From the 26 archaeological sites with known coordinates and human presence from the Early Pleistocene (see Supplementary Material Text S1), 215,306 slope values were obtained due to each archaeological site produced a matrix of 8,281 slope values within an 8 km × 8 km area of influence. The slopes of the terrain range from 0° to 90°. This range was divided into 464 intervals, defined by the square root rule.

Figure S3

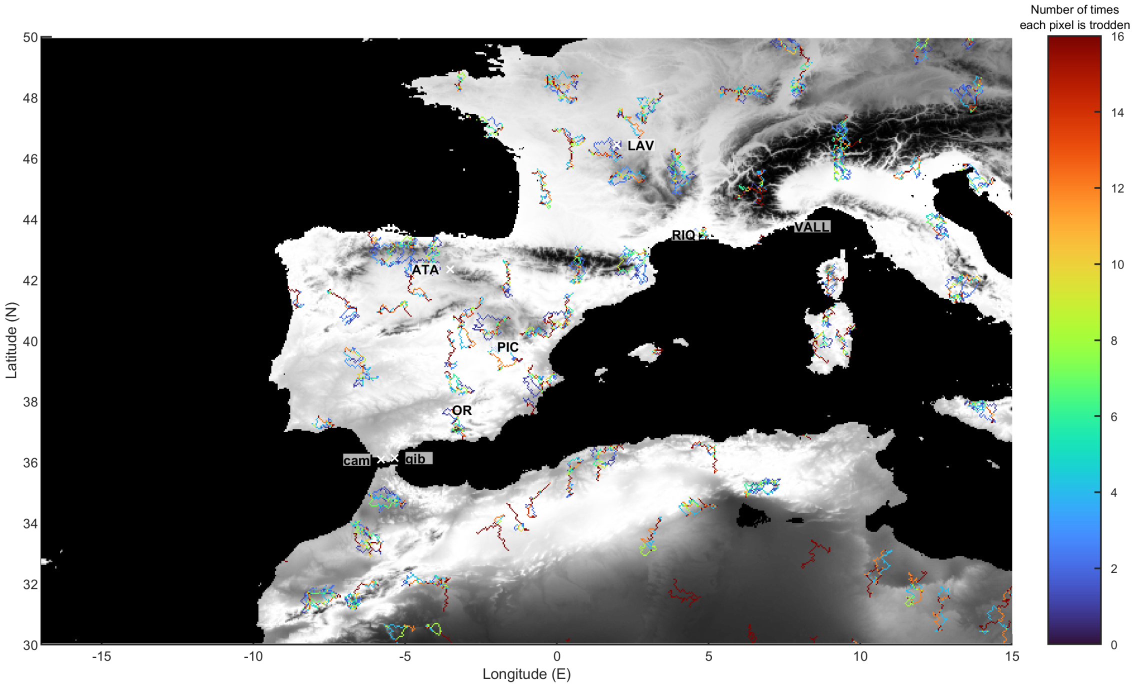

Figure S3. Example of results for a set (here, set 325). The map shows the result for only one set, which corresponds to running the Rihla algorithm 16 times on 100 pairs of points (start and end). The colors indicate the number of times each pixel was trodden in the specific set number 325.

Figure S4

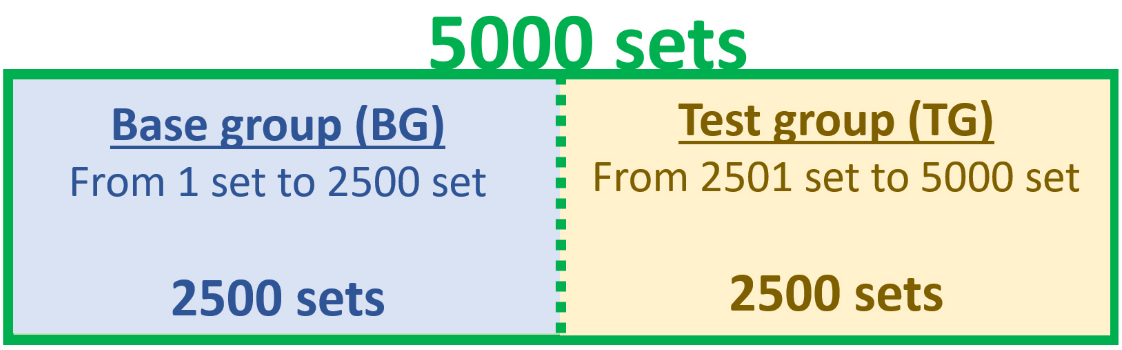

Figure S4. Division of the 5,000 sets into groups. The 5,000 sets were divided into two groups: the Base group (BG) with the first 2,500 sets (1–2,500) and the Test group (TG) with the next 2,500 sets (2,501–5,000).

Figure S5

$$
\underset{M}{\begin{array}{|c|c|c|c|c|}\hline 3 & 5 & 3 & 7 & 2 \\ \hline 7 & 12 & 4 & 3 & 3 \\ \hline 5 & 2 & 10 & 14 & 5 \\ \hline 7 & 3 & 1 & 6 & 2 \\ \hline 11 & 3 & 2 & 1 & 4 \\ \hline \end{array}}
\xrightarrow{mn_{i,j} = \frac{m_{i,j}}{\sum m_{i,j}}}
\underset{MN}{\begin{array}{|c|c|c|c|c|}\hline \frac{3}{125} & \frac{5}{125} & \frac{3}{125} & \frac{7}{125} & \frac{2}{125} \\ \hline \frac{7}{125} & \frac{12}{125} & \frac{4}{125} & \frac{3}{125} & \frac{3}{125} \\ \hline \frac{5}{125} & \frac{2}{125} & \frac{10}{125} & \frac{14}{125} & \frac{5}{125} \\ \hline \frac{7}{125} & \frac{3}{125} & \frac{1}{125} & \frac{6}{125} & \frac{2}{125} \\ \hline \frac{11}{125} & \frac{3}{125} & \frac{2}{125} & \frac{1}{125} & \frac{4}{125} \\ \hline \end{array}}
$$

Figure S5. Synthetic example of the map normalization process. The original map, called M, contains the number of times each pixel was trodden. To obtain the normalized map, called MN, each value of M, called $m_{i,j}$, is divided by the total sum of all values in M, called $\sum m_{i,j}$, following Equation 1. Thus, each element de MN, called $nm_{i,j}$, represents the relative proportion of times pixel i, j was trodden with respect to the total number of trodden recorded in the map.

Figure S6

$$
\left.\begin{array}{c}
BMN \\
\begin{array}{|c|c|c|c|c|}\hline \frac{4}{150} & \frac{7}{150} & \frac{1}{150} & \frac{3}{150} & \frac{5}{150} \\ \hline \frac{7}{150} & \frac{12}{150} & \frac{5}{150} & \frac{3}{150} & \frac{3}{150} \\ \hline \frac{5}{150} & \frac{2}{150} & \frac{10}{150} & \frac{14}{150} & \frac{15}{150} \\ \hline \frac{8}{150} & \frac{7}{150} & \frac{1}{150} & \frac{6}{150} & \frac{2}{150} \\ \hline \frac{11}{150} & \frac{2}{150} & \frac{7}{150} & \frac{1}{150} & \frac{9}{150} \\ \hline \end{array} \\
TMN \\
\begin{array}{|c|c|c|c|c|}\hline \frac{3}{138} & \frac{8}{138} & \frac{5}{138} & \frac{3}{138} & \frac{4}{138} \\ \hline \frac{2}{138} & \frac{1}{138} & \frac{5}{138} & \frac{12}{138} & \frac{3}{138} \\ \hline \frac{5}{138} & \frac{6}{138} & \frac{12}{138} & \frac{2}{138} & \frac{5}{138} \\ \hline \frac{8}{138} & \frac{8}{138} & \frac{7}{138} & \frac{4}{138} & \frac{21}{138} \\ \hline \frac{3}{138} & \frac{2}{138} & \frac{7}{138} & \frac{1}{138} & \frac{1}{138} \\ \hline \end{array}
\end{array}\right\}
\xrightarrow{DoS = mean\left(100\,\frac{tmn_{i,j}}{bmn_{i,j}}\right)}
DoS = mean
\begin{array}{|c|c|c|c|c|}\hline
100\left(\frac{3}{138}:\frac{4}{150}\right) & 100\left(\frac{8}{138}:\frac{7}{150}\right) & 100\left(\frac{5}{138}:\frac{1}{150}\right) & 100\left(\frac{3}{138}:\frac{3}{150}\right) & 100\left(\frac{4}{138}:\frac{5}{150}\right) \\ \hline
100\left(\frac{2}{138}:\frac{7}{150}\right) & 100\left(\frac{1}{138}:\frac{12}{150}\right) & 100\left(\frac{5}{138}:\frac{5}{150}\right) & 100\left(\frac{12}{138}:\frac{3}{150}\right) & 100\left(\frac{3}{138}:\frac{3}{150}\right) \\ \hline
100\left(\frac{5}{138}:\frac{5}{150}\right) & 100\left(\frac{6}{138}:\frac{2}{150}\right) & 100\left(\frac{12}{138}:\frac{10}{150}\right) & 100\left(\frac{2}{138}:\frac{14}{150}\right) & 100\left(\frac{5}{138}:\frac{15}{150}\right) \\ \hline
100\left(\frac{8}{138}:\frac{8}{150}\right) & 100\left(\frac{8}{138}:\frac{7}{150}\right) & 100\left(\frac{7}{138}:\frac{1}{150}\right) & 100\left(\frac{4}{138}:\frac{6}{150}\right) & 100\left(\frac{21}{138}:\frac{2}{150}\right) \\ \hline
100\left(\frac{3}{138}:\frac{11}{150}\right) & 100\left(\frac{2}{138}:\frac{2}{150}\right) & 100\left(\frac{7}{138}:\frac{7}{150}\right) & 100\left(\frac{1}{138}:\frac{7}{150}\right) & 100\left(\frac{1}{138}:\frac{9}{150}\right) \\ \hline
\end{array}
$$

Figure S6. Synthetic example of the calculation of the degree of similarity (DoS) between two normalized maps. The normalized base map, called BMN, and the normalized test map, called TMN, are compared pixel by pixel using Equation 2. The DoS is obtained as the mean of the ratios between corresponding values of both maps, multiplied by 100. A DoS value of 100 indicates a perfect match between maps, whereas values deviating from 100 (either higher or lower) reflect greater divergence in the distribution of trodden pixels across the two maps.

Figure S7

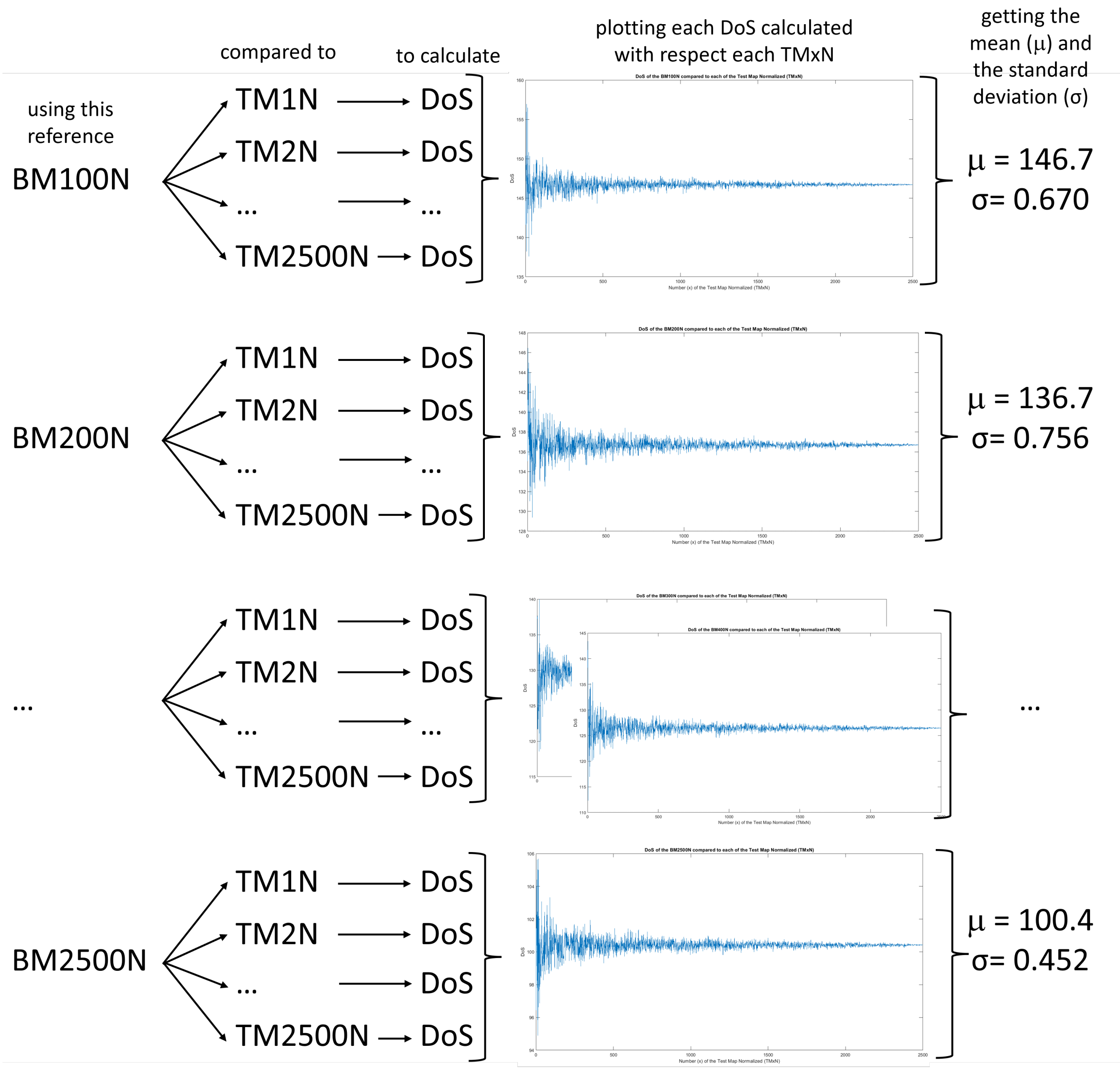

Figure S7. Schematic representation of the comparison process between normalized base maps and normalized test maps. Each BMxN was compared with all TMxN, yielding one Degree of Similarity (DoS) value per comparison. For example, BM100N was compared with TM1N to TM2500N, resulting in 2,500 DoS values. The procedure was repeated for each BM, leading to a total of 62,500 comparisons. This figure illustrates the DoS values obtained for selected BMs (BM100N, BM200N, …, BM2500N), showing their mean (μ) and standard deviation (σ). As the number of sets increased, the base maps converged toward the test maps, with BM2500N (constructed from the maximum number of sets) selected as the reference Base Map (BaM) for subsequent analyses.

Figure S8

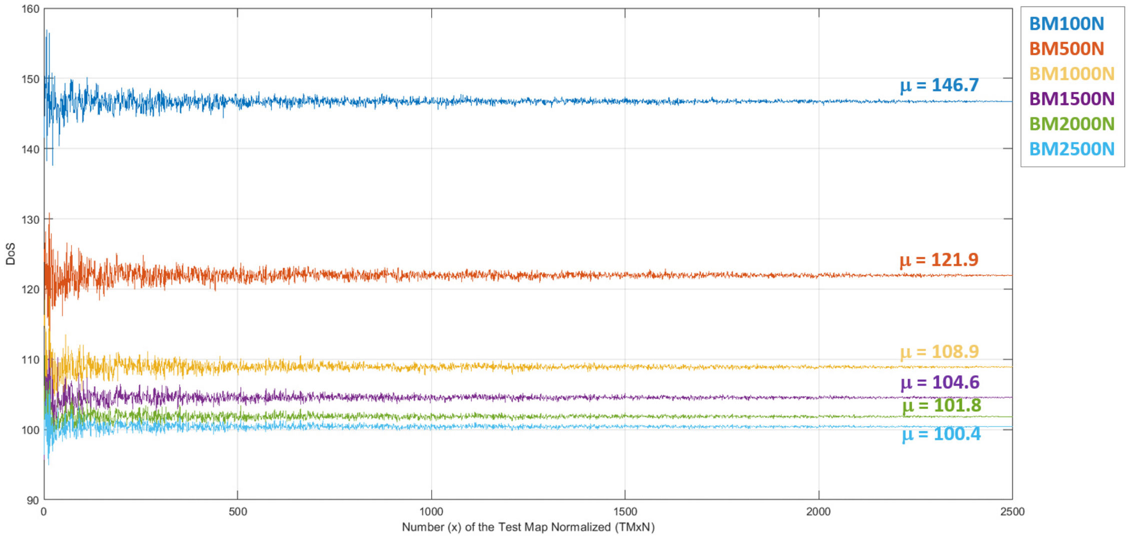

Figure S8. Degree of similarity (DoS) values of selected normalized base maps normalized compared with all normalized test maps. BM100N, BM500N, BM1000N, BM1500N, BM2000N, and BM2500N were compared against TM1N to TM2500N, resulting in 2,500 DoS values per BMN. The mean (μ) of the DoS values is shown for each BMN. As the number of sets increases, the BMNs converge toward the TMNs, with BM2500N showing the closest agreement (μ=100.4). This confirms that BM2500N, generated from the largest number of sets, serves as the most reliable reference Base Map (BaM) for subsequent analyses.

Figure S9

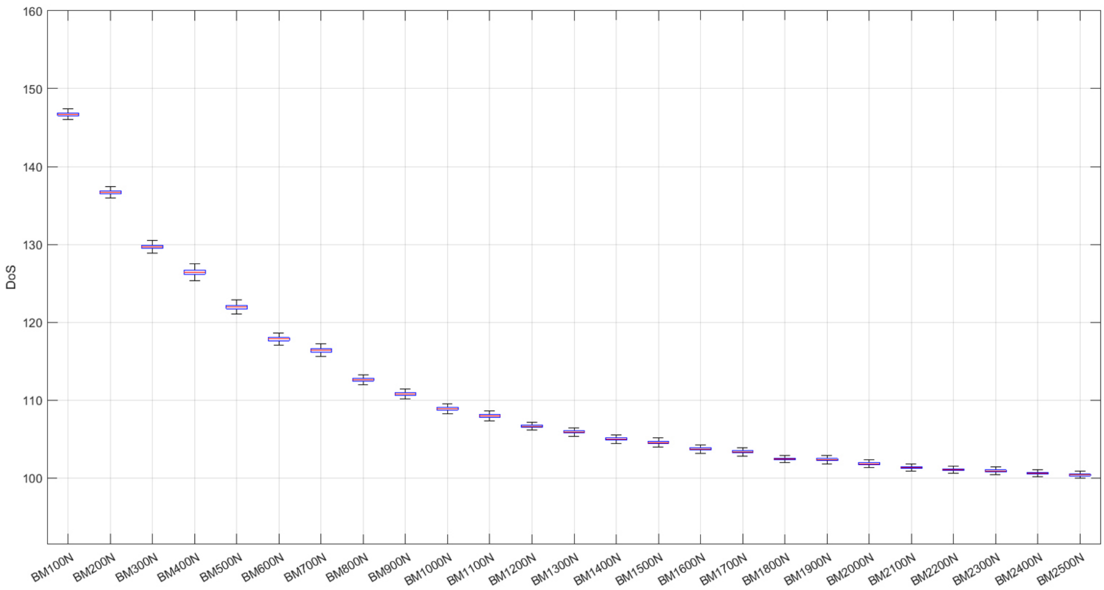

Figure S9. Boxplot representation of the Degree of Similarity (DoS) values obtained when each normalized base map was compared with all normalized test maps. Each BM produced 2,500 DoS values, resulting in a total of 62,500 comparisons. The figure illustrates how the DoS decreases and stabilizes as the number of sets increases, reflecting the convergence of base maps toward test maps. When using the maximum number of sets (2,500), the variability fell below 0.4% (DoS=100.4%), confirming BM2500N as the most consistent and reliable reference Base Map (BaM) for subsequent analyses.

Figure S10

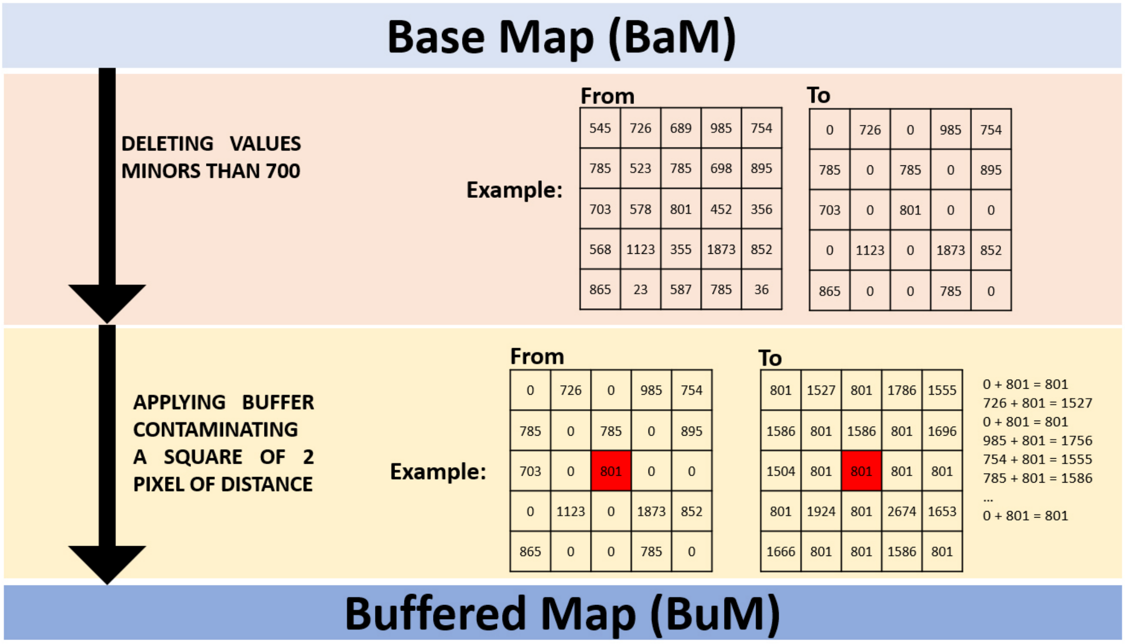

Figure S10. Synthetic example of the calculation of the buffered base map (BuM). Two sequential filtering steps were applied to the base map (BaM). First, only pixels with values greater than 700 were retained, while all others were set to zero. Second, a buffering operation was performed, expanding the influence of each retained pixel into a surrounding 8-pixel square. All pixels within this neighborhood were assigned the value of the central pixel. These steps improved the visualization and spatial continuity of the BaM results, generating the final buffered map (BuM).

Figure S11

(a) Sample example of a submap of any connectivity map (CoM) for a spatial density of trodden greater than 50

0	1	2	3
2	5	7	3
1	5	5	2
2	7	7	54
3	3	9	5
60	40	9	45
70	47	5	8
3	1	5	104

$$Patch\ resulting\ from\ the\ following: \frac{54}{1} > 50$$

$$Patch\ resulting\ from\ the\ following: \frac{104+8}{2} > 50$$

$$Patch\ resulting\ from\ the\ following: \frac{60+70+40+47}{4} > 50$$

Patch I
Patch II
Patch III

(b) Sample example of calculating the percentage of land trodden (PoLT) for the same submap as in (a)
(submap from any connectivity map with a spatial density of trodden greater than 50)

0	1	2	3
2	5	7	3
1	5	5	2
2	7	7	**54**
3	**3**	9	5
60	**40**	9	45
70	47	5	**8**
3	1	5	**104**

$$PoLT = 100\,\frac{number\ of\ trodden\ pixel}{number\ of\ land\ pixel} = 100\,\frac{1+4+2}{24} \approx 29\ \%$$

Land
Ocean

Note: The fact that the pixel number is in bold and displayed in red, green, or purple indicates that the pixel is part of a patch

Figure S11. Synthetic example of the calculation of connectivity maps (CoMs) and the percentage of land trodden (PoLT). (a) Example of patch formation in a submap, where a patch is defined as a group of connected pixels whose trodden density (calculated as the ratio of the cumulative trodden values of a pixel and its eight immediate neighbours to the number of pixels in the patch) exceeds a predefined threshold. Different colours indicate distinct patches. (b) Example of PoLT calculation for the same submap, obtained as the ratio between the number of trodden pixels and the total number of land pixels. These simplified examples illustrate the methodological steps used to generate the 16,630 CoMs and their associated PoLT values.

Figure S12

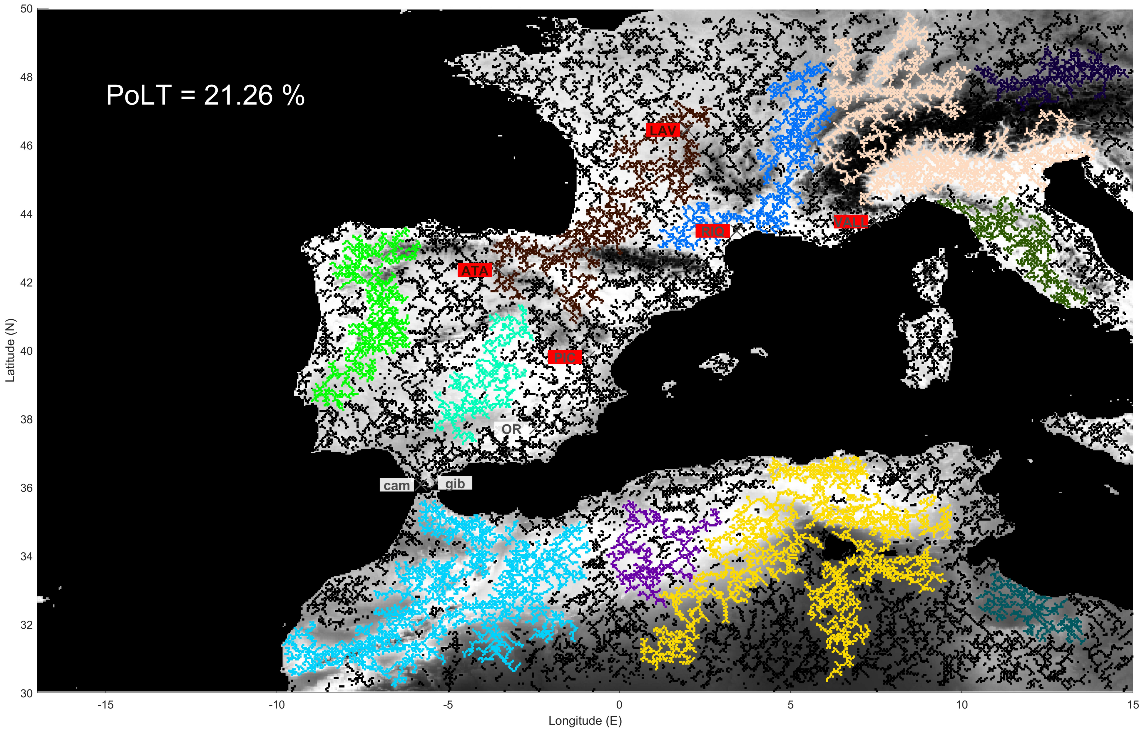

Figure S12. Representative connectivity map (CoM) with its corresponding percentage of land trodden (PoLT). Each continuous patch within the CoM was identified using the connected components on multilabel 3D images (cc3d) algorithm, which assigns a unique colour to each group of connected pixels. The PoLT was computed as the ratio of trodden pixels to the total number of land pixels. In this example, corresponding to a minimum spatial trodden density of 15,666, the calculated PoLT is 21.26%. For clarity, only patches larger than 500 pixels were assigned colours other than black, highlighting the most significant areas. Archaeological sites marked in red are connected, indicating that their locations can be traversed via a continuous path.

TABLES

Table S1. Archaeological sites from the Early Pleistocene with known coordinates and evidence of human presence. The table lists the 26 sites used for the terrain slope analysis, including their location, country, chronological dating, dating technique(s), geographic coordinates (latitude, longitude), altitude, and bibliographic reference from which the information was obtained. These coordinates served as the basis for downloading the corresponding digital elevation models (DEMs).

The file Table S1.xlsx is available for download at the following link:
https://drive.google.com/drive/folders/1eGdx3-uYNctL8UkU-zm3wcVS4EC7LHtE?usp=sharing

Table S2. Terrain slope values extracted from the area of influence surrounding each of the 26 Early Pleistocene archaeological sites. For each archaeological site, a subraster of 91 × 91 pixels (approximately 8 km × 8 km) was generated from the DEM, yielding 8,281 slope values per site and a total of 215,306 slope values across all sites analysed. The header of each row indicates the pixel position relative to the central pixel corresponding to each archaeological site: he first value in the parenthesis refers to the horizontal axis (positive to the right), and the second value refers to the vertical axis (positive downward).

The file Table S2.xlsx is available for download at the following link:
https://drive.google.com/drive/folders/1eGdx3-uYNctL8UkU-zm3wcVS4EC7LHtE?usp=sharing

Table S3. Pixel values of the Base Map (BaM). The row and column headers represent latitude and longitude, respectively, in geographic coordinates. Each cell value corresponds to the number of times the specific pixel was trodden, summing across the first 2,500 sets.

The file Table S3.xlsx is available for download at the following link:
https://drive.google.com/drive/folders/1eGdx3-uYNctL8UkU-zm3wcVS4EC7LHtE?usp=sharing

Table S4. Pixel values of the Buffered Map (BuM). The row and column headers represent latitude and longitude, respectively, in geographic coordinates. Each cell value corresponds to the number of times the specific pixel was trodden, summing across the first 2,500 sets after applying the filtering procedure to the BaM. This procedure consisted of two sequential steps: (i) retaining only pixels with values greater than 700, setting all others to zero; and (ii) applying a buffering operation to extend the influence of the retained pixels to their neighbouring areas. Each retained pixel was expanded in all directions to form an 8-pixel square, and all pixels within this region were assigned the value of the central pixel.

The file Table S4.xlsx is available for download at the following link:
https://drive.google.com/drive/folders/1eGdx3-uYNctL8UkU-zm3wcVS4EC7LHtE?usp=sharing

Table S5. Presence–absence matrix of faunal assemblages across nine regions (SW Europe, W Europe, SE Europe, Ponto-Caspian, Anatolia, Levant, North Africa, E Africa [Shungura], and China [Nihewan]). Rows represent regions, and columns represent faunal taxa. Each cell is coded as 1 when the taxon is present in the corresponding region and 0 when it is absent.

The file Table S5.xlsx is available for download at the following link:
https://drive.google.com/drive/folders/1eGdx3-uYNctL8UkU-zm3wcVS4EC7LHtE?usp=sharing

TEXT

Text S1: Palaeontological sites used in the analysis of similarity among faunal assemblages

To evaluate the similarity among faunal assemblages from different geographical regions during the early Pleistocene, we carried out a correspondence analysis (see Methods) that included 76 faunal assemblages (> 5 taxa) corresponding to 69 palaeontological sites with chronologies between 2.5 and 0.9 Ma (Table S6). From a taxonomical point of view, we included 136 genera (Supplementary Information Table S5). The goal of this analysis was to assess the similarity between faunal assemblages in northern Africa and southwestern Europe.

The following regions were included (number of faunal assemblages in parentheses) (Table S6 and Table S7): southwestern Europe (23), western Europe (11), southeastern Europe (6), Ponto-Caspian (4), Anatolian (5), Levant (4), northern Africa (13), the Shungura Formation (levels D-L), which is representative of eastern Africa, and the Nihewan Basin (8), which is representative of China.

Despite being relatively modern (0.9 Ma) (Gibert et al., 2016), the site of Cueva Victoria (Murcia, SE Iberian Peninsula) was included because it is the only European site where the African genus *Theropithecus* has been recorded (Ferràndez-Cañadell et al., 2014).

Region	Number of sites	Number of assemblages
SW Europe	24	24
W Europe	9	11
SE Europe	6	6
Ponto-Caspian	4	4
Anatolia	5	5
Levant	3	4
N Africa	9	13
E Africa (Shungura)	1	1
China (Nihewan Basin)	8	8
Total	**69**	**76**

Table S6. Number of sites by region included in the similarity analysis. In the case of W Europe, 3 faunal assemblages were obtained from Saint Vallier; 2 faunal assemblages were obtained from the Levantine site of Ubeidiyya; and 2 faunal assemblages were obtained from the North African sites of Ain Boucherit, El Kherba, and Thomas Quarry (see Table S6). For all other sites, 1 faunal assemblage was obtained.

Site	Region	Chronology (Ma)	Reference
Vallonet Complex III	SW Europe	1.1	Michel et al. (2017)
Slivia	SW Europe	2.6-0.78	NOW Community
Poggio Rosso	SW Europe	1.95-1.8	NOW Community
Pirro Nord	SW Europe	1.86-1.13	NOW Community

Pietrafitta	SW Europe	1.9-1.43	NOW Community
Pantalla	SW Europe	2.2	Cherin et al. (2023)
Olivola	SW Europe	2.1-1.98	NOW Community
Monte Argentario	SW Europe	1.9-1.4	NOW Community
Matassino	SW Europe	1.98-1.88	NOW Community
Farneta	SW Europe	1.86-1.68	NOW Community
Colle Curti	SW Europe	2.6-0.78	NOW Community
Casa Frata	SW Europe	2.6-0.78	NOW Community
La Puebla de Valverde	SW Europe	2.5	NOW Community
Quibas	SW Europe	1.1	Rosas et al. (2022)
Fuente Nueva 3	SW Europe	1.2	Yravedra et al. (2024)
Barranco León	SW Europe	1.46	Toro-Moyano et al. (2013)
Venta Micena	SW Europe	1.6	Luzón et al. (2021)
Huélago	SW Europe	2.5	Alberdi et al. (2001)
Fonelas P-1 (Trench B)	SW Europe	2.0	Arribas et al. (2009)
Montopoli	SW Europe	2.2-2.0	Bartolini-Lucenti et al. (2022)
Atapuerca TD4-5	SW Europe	1.1-0.8	Rodríguez-Gómez et al. (2022)/NOW Community
Atapuerca TE9	SW Europe	1.2	Carbonell et al. (2008)
Cueva Victoria	SW Europe	0.9	Gibert et al. (2016)
Almenara-Casablanca 1	SW Europe	2.5-1.9	NOW Community
Senèze	W Europe	2.2-2.1	NOW Community
Sainzelles	W Europe	2.5-1.9	NOW Community
Saint Vallier Banc LD3	W Europe	2.5-1.9	NOW Community
Saint Vallier Banc LD2	W Europe	2.5-1.9	NOW Community
Saint Vallier	W Europe	2.5-1.9	NOW Community
Roca Neyra	W Europe	2.5	NOW Community

Pardines	W Europe	2.5-1.8	NOW Community
Coupet	W Europe	2.5-1.9	NOW Community
Cornillet 3	W Europe	2.5-1.9	NOW Community
Chilhac	W Europe	2.5-1.9	NOW Community
Tegelen	W Europe	2.4-1.7	O'Regan & Turner (2004)
Trlica 11-10	SE Europe	1.8-1.2	Vislobokovan & Agadjanian (2016)
Fântâna lui Mitilan	SE Europe	1.6 (1.7-1.5)	Terhune et al. (2020)
Grăunceanu	SE Europe	1.94 (2.05-1.87)	Terhune et al. (2020)
Vatera	SE Europe	2.5-1.9	NOW Community
Apollonia 1	SE Europe	1.2-1.0	Koufos (2018) (Carnivores) / NOW Community
Tsiotra Vryssi	SE Europe	2.4-1.7	Konidaris et al. (2015)
Dmanisi	Ponto-Caspian	1.8	Cappellini et al. (2019)
Kotsakhuri	Ponto-Caspian	2.5-1.9	NOW Community
Tsalka	Ponto-Caspian	2.3-1.5	Nomade et al. (2016)
Akhalkalaki	Ponto-Caspian	0.9-0.7	Tappen et al. (2002)
Kocabaş	Anatolia	1.6-1.2	Rausch et al. (2019)
Yukarisögutönu	Anatolia	1.9-0.01	NOW Community
Sarikol Tepe	Anatolia	2.5-1.9	NOW Community
Kamisli	Anatolia	1.9-0.01	NOW Community
Dursunlu	Anatolia	1.9-0.01	Güleç et al. (2009)/Now Community
Latamne	Levant	1.9-0.01	NOW Community
Evron Quarry	Levant	1.14-0.78	NOW Community
Ubeidiya	Levant	1.9-1.2	NOW Community

Ubeidiya Layer II 23	Levant	1.8-1.1	Barash et al. (2023)
Ain Boucherit AB-Lw	N Africa	2.44	Duval et al. (2021)
Ain Boucherit AB-Up	N Africa	1.92	Duval et al. (2021)
El Kherba	N Africa	1.75	Duval et al. (2021)
El Kherba Puits	N Africa	1.75	Duval et al. (2021)
Ain Hanech	N Africa	1.75	Duval et al. (2021)
Mansourah	N Africa	1.8	Chaid-Saoudi et al. (2006)
Tighenif	N Africa	1.0	NOW Community
Ahl al Oughlam	N Africa	2.4-2.0	Geraads et al. (1998)
Thomas Quarry 1 (HEC)	N Africa	1.7	NOW Community
Thomas Quarry 1 (L)	N Africa	2.6-0.78	NOW Community
El Geffel	N Africa	2.6-0.78	NOW Community
Wadi Sarrat	N Africa	2.6-0.78	Martínez-Navarro et al. (2014)
Guefaït 4	N Africa	2.4	Ramírez et al. (2024)
Shungura Formation	E Africa	2.5-1.2	NOW Community
Hongya	China (Nihewan Basin)	2.4	Ao et al. (2013)
Xiashagou	China (Nihewan Basin)	1.7-2.2	Ao et al. (2013)
Huabaogou	China (Nihewan Basin)	1.9-1.7	Ao et al. (2013)
Yangshuizhan	China (Nihewan Basin)	1.8-1.6	Ao et al. (2013)
Majuangou	China (Nihewan Basin)	1.66-1.6	Ao et al. (2013)
Xiaochangliang	China (Nihewan Basin)	1.36	Ao et al. (2013)
Banshan	China (Nihewan Basin)	1.32	Ao et al. (2013)

Dongguttuo	China (Nihewan Basin)	1.1	Ao et al. (2013)

Table S7. Early Pleistocene sites with faunal assemblages included in the similarity analysis.

References

Alberdi, M.T., Alonso, M.A., Azanza, B., Hoyos, M., Morales, J. (2001) Vertebrate taphonomy in circum-lake environments: three cases in the Guadix-Baza Basin (Granada, Spain). *Palaeogeography, Palaeoclimatology, Palaeoecology* **165**: 1-26

Ao, H., An, Z.S., Dekkers, M.J., Li, Y.X., Xiao, G.Q., Zhao, H., Qiang, X.K., (2013) Pleistocene magnetochronology of the fauna and Paleolithic sites in the Nihewan Basin: significance for environmental and hominin evolution in North China. *Quaternary Geochronology* **18**: 78-92

Arribas, A., Garrido, G., Viseras, C., Soria, J. M., Pla, S., García, J., Garcés, M., Beamud, E., & Carrión, J. S. (2009) A mammalian lost world in southwest Europe during the Late Pliocene. *PLoS ONE* **4**: 7127

Barash, A., Belmaker, M., Bastir, M., Soudack, M., O'Brien, H.D., Woodward, H., Prendergast, A., Barzilai, O., Been, E. (2022) The earliest Pleistocene record of a large-bodied hominin from the Levant supports two out-of-Africa dispersal events. *Scientific Reports* **12**: 1721

Bartolini-Lucenti, S., Cirilli, O., Pandolfi, L., Rook, L. (2022) The Montopoli site, a reference local fauna in the Pliocene and pleistocene European large mammals biochronology, first discovered by Giovanni Capellini (1833-1922). *Bollettino della Società Paleontologica Italiana* **61**: 207-222

Cappellini, E., Welker, F., Pandolfi, L., Ramos-Madrigal, J., Samodova, D., Rüther, P.L., Fotakis, A.K., Lyon, D., Moreno-Mayar, J.V., Bukhsianidze, M., Jersie-Christensen, R. R., Mackie, M., Ginolhac, A., Ferring, R., Tappen, M., Palkopoulou, E., Dickinson, M. R., Stafford, T.W., Chan, Y.L., Götherström, A., Nathan, S.K.S.S., Heintzman, P.D., Kapp, J.D., Kirillova, I., Moodley, Y., Agustí, J., Kahlke, R.-D., Kiladze, G., Martínez–Navarro, B., Liu, S., Velasco, M.S., Sinding, M.-H.S., Kelstrup, C.D., Allentoft, M.E., Orlando, L., Penkman, K., Shapiro, B., Rook, L., Dalén, L., Gilbert, M.T.P., Olsen, J.V., Lordkipanidze, D., Willerslev, E. (2019) Early Pleistocene enamel proteome sequences from Dmanisi resolves *Stephanorhinus* phylogeny. *Nature* **574**: 103-107

Carbonell, E., Bermúdez De Castro, J.M., Parés, J.M., Pérez-González, A., Cuenca-Bescós, G., Ollé, A., Mosquera, M., Huguet, R., Van Der Made, J., Rosas, A., Sala, R., Vallverdú, J., García, N., Granger, D.E., Martinón-Torres, M., Rodríguez, X.P., Stock, G.M., Vergès, J.M., Allué, E., Burjachs, F., Cáceres, I., Canals, A., Benito, A., Díez, C., Lozano, M., Mateos, A., Navazo, M., Rodríguez, J., Rosell, J., Arsuaga, J.L. (2008) The first hominin of Europe. *Nature* **452**: 465-469

Chaid-Saoudi, Y., Geraads, D., Raynal, J.P. (2006) The fauna and associated artefacts from the Lower Pleistocene site of Mansourah (Constantine, Algeria). *Comptes Rendus Palevol* **5**: 963-971

Cherin, M., Basilici, G., Duval, M., Shao, Q., Sier, M.J., Parés, J.M., Gliozzi, E., Mazzini, I., Magri, D., Di Rita, F., Iurino, D.A., Azzarà, B., Margaritelli, G., Pazzaglia, F. (2023) The dawn of the late Villafranchian: Paleoenvironment and age of the Pantalla paleontological site (Italy; early Pleistocene). *Quaternary Science Reviews* **316**: 108279

Duval, M., Sahnouni, M., Parés, J.M., van der Made, J., Abdessadok, S., Harichane, Z., Chelli Cheheb, R., Boulaghraif, K., Pérez-González, A. (2021) The Plio-Pleistocene sequence of Oued Boucherit (Algeria): a unique chronologically-constrained archaeological and paleontological record in North Africa. *Quaternary Science Reviews* **271**: 107-116

Ferràndez-Cañadell, C., Ribot, F., Gibert, L. (2014) New fossil teeth of *Theropithecus oswaldi* (Cercopithecoidea) from the Early Pleistocene at Cueva Victoria (SE Spain). *Journal of Human Evolution* **74**: 55-66

Geraards, D., Amani, F., Raynal, J.-P., Sbihi-Alaoui, F.Z. (1998) La faune de Mammifères du Pliocène terminal d'Ahl al Oughlam, Casablanca, Maroc. *Comptes Rendus Hebdomadaires des Séances de l'Académie des Sciences* **326**: 671-676

Gibert, L., Scott, G.R., Scholz, D., Budsky, A., Ferràndez, C., Ribot, F., Martin, R.A., Lería, M. (2016) Chronology for the Cueva Victoria fossil site (SE Spain): Evidence for Early Pleistocene Afro-Iberian dispersals. *Journal of Human Evolution* **90**: 183-197

Güleç, E., White, T., Kuhn, S., Özer, I., Sağir, M., Yilmaz, H., Clark Howell, F. (2002) The Lower Pleistocene lithic assemblage from Dursunlu (Konya), Central Anatolia, Turkey. *Antiquity* **83**: 11-22

Konidaris, G.E., Tourloukis, V., Kostopoulos, D.S., Thompson, N., Giusti, D., Michailidis, D., Koufos, G.D., Harvati, K. (2015) Two new vertebrate localities from the early Pleistocene of Mygdonia basin (Macedonia, Greece): preliminary results. *Comptes Rendus Palevol* **14**: 353-362

Koufos, G.D. (2018) New material and revision of the Carnivora, Mammalia from the Lower Pleistocene locality Apollonia 1, Greece. *Quaternary* **1**: 6

Luzón, C., Yravedra, J., Courtenay, L.A., Saarinen, J., Blain, H.-A., DeMiguel, D., Viranta, S., Azanza, B., Rodríguez-Alba, J.J., Herranz-Rodrigo, D., Serrano-Ramos, A., Solano, J.A., Oms, O., Agustí, J., Fortelius, M., Jiménez-Arenas, J.M. (2021) Taphonomic and spatial analyses from the Early Pleistocene site of Venta Micena 4 (Orce, Guadix-Baza Basin, Southern Spain). *Scientific Reports* **11**: 13977

Martínez-Navarro, B., Karoui-Yaakoub, N., Oms, O., Amri, L., López-García, J.M., Zerai, K., Blain, H.-A., Mtimet, M.-S., Espigares, M.-P., Ben Haj Ali, N., Ros- Montoya, S., Boughdiri, M., Agustí, J., Khayati-Ammar, H., Maalaoui, K., Om El Khir, M., Sala, R., Othmani, A., Hawas, R., Gómez-Merino, G., Solé, A., Carbonell, E., Palmqvist, P. (2014) The early Middle Pleistocene archae- opaleontological site of Wadi Sarrat (Tunisia) and the earliest record of Bos primigenius. *Quaternary Science Reviews* **90**: 37-46

Michel, V., Shen, C.C., Woodhead, J., Hu, H.M., Wu, C.C., Moulle, P.E ,Khatib, S., Cauche, D., Moncel, M.-H., Valensi, P., Chou, Y.-M., Gallet, S., Echassoux, A., Orange, F., de Lumley, H. (2017) New dating evidence of the early presence of hominins in Southern Europe. *Scientific Reports* **7**: 10074

Nomade, S., Scao, V., Guillou, H., Messager, E., Mgeladze, A., Voinchet, P. (2016) New 40Ar/39Ar, unspiked K/Ar and geochemical constraints on the Pleistocene magmatism of the Samtskhe-Javakheti highlands (Republic of Georgia). *Quaternary International* **395**: 45-59

NOW Community (2024) New and Old Worlds Database of Fossil Mammals (NOW). Licensed under CC BY 4.0. Retrieved 03/12/2024 from https://nowdatabase.org/now/database/

O'Regan, H.J., Turner, A. (2004) Biostratigraphic and palaeoecological implications of new fossil felid material from the Plio-Pleistocene site of Tegelen, the Netherlands. *Palaeontology* **47**: 1181-1193

Ramírez-Pedraza, I., Tornero, C., Aouraghe, H., Rivals, F., Patalano, R., Haddoumi, H., Expósito, I., Rodríguez-Hidalgo, A., Mischke, S., van der Made, J., Piñero, P., Blain, H.-A., Roberts, P., Kumar Jha, D., Agustí, J., Sánchez-Bandera, C., Lemjidi, A., Benito-Calvo, A., Moreno-Rivas, E., Oujaa, A., Mhamdi, H., Souhir, M., Aissa, A.M., Chacón, M.G., Sala-Ramos, R. (2024) Arid, mosaic environments during the Plio-Pleistocene transition and early hominin dispersals in northern Africa. *Nature Communications* **15**: 8393

Rausch, L., Alçiçek, H., Vialet, A., Boulbes, N., Mayda, S., Titov, V.V., Stoica, M., Charbonnier, S., Abels, H.A., Tesakov, A.S., Moigne, A.-M., Andrieu-Ponel, V., Franceschi, D.D., Neubauer, T.A., Wesselingh, F.P., Alçiçek, M.C. (2019) An integrated reconstruction of the early Pleistocene palaeoenvironment of *Homo erectus* in the Denizli Basin (SW Turkey). *Geobios* **57**: 77-95

Rodríguez-Gómez, G., Palmqvist, P., Martínez-Navarro, B., Martín-González, J.A., Bermúdez de Castro, J.M. (2022) Mean body size estimation in large mammals and the computation of biomass in past ecosystems: an application to the Pleistocene sites of Orce and Sierra de Atapuerca (Spain). *Comptes Rendus Palevol* **21**: 207-233

Rosas, A., Galli, A.E., Fidalgo, D., García Tabernero, A. Huguet, R., Martínez, D., Piñero, P., Agustí, J., Rico Barrio, A., Vallverdú, J. (2022) The Quibas site Murcia Spain new herbivores from the Early-Middle Pleistocene Transition. *Rivista Italiana di Paleontologia e Stratigrafia* **128**: 745-772

Tappen, M, Adler, D.S., Ferring, C.R., Gabunia, M., Vekua, A., Swisher III, C.C. (2002) Akhalkalaki: The taphonomy of an Early Pleistocene locality in the Republic of Georgia. *Journal of Archaeological Science* **29**: 1367-1391

Terhune, C.E., Curran, S., Croitor, R., Dragusin, V., Gaudin, T., Petculescu, A., Robinson, C., Robu, M., Werdelin, L. (2020) Early Pleistocene fauna of the Oltet River valley of Romania: biochronological and biogeographic implications. *Quaternary International* **553**: 14-33

Toro-Moyano, I., Martínez-Navarro, B., Agustí, J., Souday, C., Bermúdez de Castro, J.M., Martínón, M., Fajardo, B., Duval, M., Falguères, C., Oms, O., Parés, J.M., Anadón, P., Julià, R., García, J.M., Moigne, A.M., Espigares, P., Ros-Montoya, S., Palmqvist, P., 2013. The oldest human fossil in Europe, from Orce (Spain). *Journal of Human Evolution* **65**: 1-9

Vislobokova, I.A., Agadjanian, A.K. (2016) On the history of Early-Middle Pleistocene mammal faunas of the Central Balkans. *Paleontological Journal* **50**: 187-201

Yravedra, J., Courtenay, L.A., Gutiérrez-Rodríguez, M., Reinoso-Gordo, J.F., Saarinen, J., Égüez, N., Luzón, C., Rodríguez-Alba, J.J., Solano, J. A., Titton, S., Montilla-Jiménez, E., Cámara-Donoso, J., Herranz-Rodrigo, D., Estaca, V., Serrano-Ramos, A., Amorós, G., Azanza, B., Bocherens, H., DeMiguel, D., Fagoaga, A., García-Alix, A., González-Quiñones, J.J., Jiménez-Espejo, F., Kaakinen, A., Munuera, M., Ochando, J., Piñero, P., Sánchez-Bandera, C., Viranta, S., Fortelius, M., Agustí, J., Blain, H.-A., Carrión, J., Barsky, D., Oms, O., Mallol, C., Jiménez-Arenas, J.M. (2024) Not seen before. Unveiling depositional context and *Mammuthus meridionalis* exploitation at Fuente Nueva 3 (Orce, southern Iberia) through taphonomy and microstratigraphy. *Quaternary Science Reviews* **329**: 108561

VIDEO

Video S1. Connectivity maps (CoMs). The video shows the sequence of CoMs obtained iteratively from the BaM, where each CoM contains patches of connected pixels representing potential dispersal areas. Each frame corresponds to one CoM, and the percentage of land trodden (PoLT) is indicated, representing the ratio of trodden pixels to total land pixels. This stratified visualization illustrates how connectivity patterns change as a function of traffic density.

The file Connectivity Video.mp4 is available for download at the following link: https://drive.google.com/drive/folders/1eGdx3-uYNctL8UkU-zm3wcVS4EC7LHtE?usp=sharing